

# Accurate measurement of high resolution spectrum obtained by F–P etalon and ICCD

Yong Ma · Yin Yu · Hao Li · Jun Huang ·  
Yuan Yao · Bo Zhou · Yu Fang · Jun Min ·  
Kun Liang

Received: 7 August 2013 / Accepted: 21 November 2013 / Published online: 6 December 2013  
© Springer-Verlag Berlin Heidelberg 2013

**Abstract** The Fabry–Pérot (F–P) etalon and intensified charge-coupled device (ICCD) can be used to obtain the scattering spectrum and retrieve the medium parameters. However, the instrumental broadening, along with the noise, which is mainly caused by the quantum nature of the scattered light and thermally generated electrons in ICCD, will affect the measurement accuracy of the spectrum characteristics. In this paper, the characteristics of these influencing factors are analyzed, and a processing method is proposed for accurate measurement. Experiment results show that the method can improve the measurement accuracy from tens of MHzs to MHz magnitude.

## 1 Introduction

Rayleigh scattering and Brillouin scattering are series of elastic and inelastic scattering events in which light interacts with optical density variations. The results are changes in energy (frequency) and path of the photon. When the interaction is performed as elastic collision, the photon has no loss on energy but only changed on path. This scattering is called Rayleigh scattering. When the interaction is manifested as inelastic collision, the photon may lose

energy to create a quasiparticle or gain energy by destroying one. This procedure is called Brillouin scattering [1]. The frequency change is called Brillouin shift, and the spectral broadening caused by the interaction can be manifested as the full width at half maximum (FWHM) of the Brillouin peak, i.e., Brillouin linewidth. The density variations may be caused by acoustic modes, magnetic modes or temperature gradients.

Rayleigh–Brillouin scattering (RBS) is important for the measurement applications of the transparent media, such as optical fibers [2, 3], air [4–6] and water [7, 8]. In the ocean remote sensing, the RBS lidar system can measure the ocean temperature, salinity, etc., by obtaining the Brillouin shift and/or linewidth from the RBS signal. Among current methods for receiving the ocean RBS signal, the edge technique [9, 10] cannot obtain the scattering spectrum; the scanning Fabry–Pérot (F–P) interferometer [11, 12] requires long scanning time, and therefore, they have limited applications. The F–P etalon combined with intensified charge-coupled device (ICCD) can rapidly obtain the whole spectrum and has more capability in remote sensing applications [13, 14].

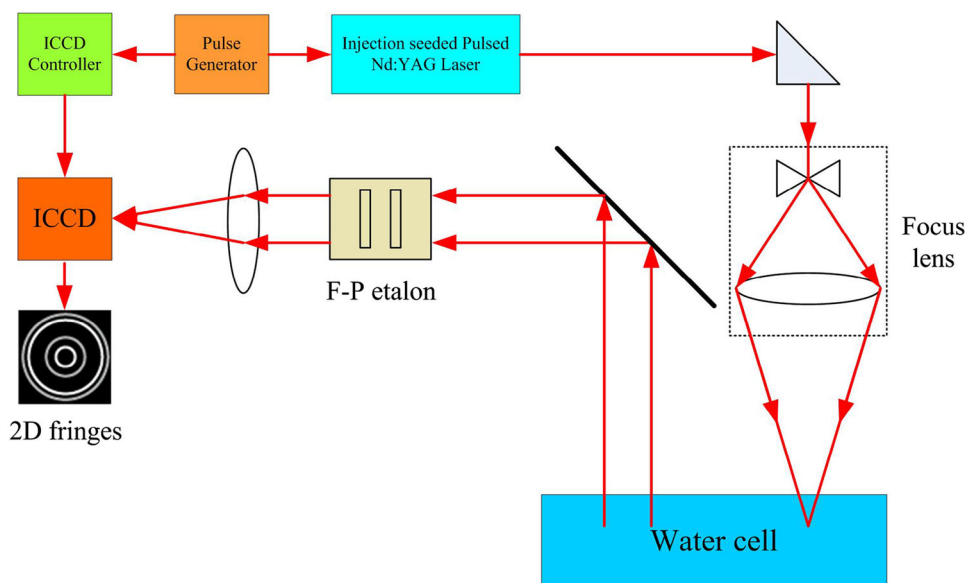
The backscattered signal obtained by F–P etalon and ICCD is displayed as 2D fringe pattern, which needs to be transformed into a 1D RBS spectrum [15]. In this procedure, the pixel resolution (corresponding to 100 MHz per pixel [16]) is the major factor limiting the measurement and characterization of the RBS spectrum. Other important factors impacting on the measurement accuracy are instrumental broadening and noise of ICCD. Since instrument transmission function is not an ideal delta function, it will broaden the received spectrum. On the other hand, the existence of noise will change the intensity of each pixel, affect the RBS spectrum profile and introduce error to the measurement of the spectrum characteristics. When image

---

Y. Ma · Y. Yu · H. Li · J. Huang · B. Zhou · Y. Fang ·  
J. Min · K. Liang (✉)  
Department of Electronics and Information Engineering,  
Huazhong University of Science and Technology,  
Wuhan 430074, People's Republic of China  
e-mail: liangkun@hust.edu.cn

Y. Yao  
College of Public Administration, Huazhong University  
of Science and Technology, Wuhan 430074,  
People's Republic of China

**Fig. 1** Scheme of the Brillouin lidar system using F-P etalon and ICCD



processing is not performed, commonly the obtained spectrum is directly used for the measurement, while the broadening and noises are overlooked [13, 15].

In our previous works, an image processing method was proposed to obtain a high resolution spectrum. The method takes full use of the statistical information provided by large amount of pixels around Rayleigh and Brillouin rings, and effectively improved the spectrum resolution from more than 100 MHz to MHz magnitude [16]. For such a high resolution spectrum, the broadening and noises should be reconsidered to improve the measurement accuracy.

In earlier research on the F-P etalon instrument, Leidecker et al. [17] had theoretically predicted the effect of the F-P etalon instrument broadening on the spectrum line shape and gave the methods for removing it. However, no detailed experiments and quantitative analysis dealing with the high resolution spectrum were done before. Besides, there are also large amount of research on the denoising methods for the 2D image obtained by ICCD [18, 19]. These methods have good performance on reducing the image noise. Unfortunately, the 1D spectrum characters obtained by these methods still have large errors. It is because these methods mainly focus on improving the image quality. They reduce the noise at the cost of distorting the original line shape that we care the most. For our application, the distortion on the spectrum will lead to the measurement error of the spectrum characteristics. These methods based on the 2D image may not be suitable for the denoising the RBS spectrum.

Therefore, the aim of this paper is to develop a suitable processing method to reduce the influence of broadening and noises for the high resolution spectrum and improve the measurement accuracy of Brillouin shift and Brillouin linewidth. Firstly, theoretical models and simulation of

broadening and noises are given. And then, a suitable processing method is proposed. Finally, the reliability of this method and the measurement accuracy of the spectrum characteristics are tested with the underwater RBS experiments.

## 2 Experimental setup

The RBS spectrum of the water is performed by the Brillouin lidar system using F-P etalon and ICCD. Figure 1 shows the configuration of this system.

The underwater experiments are based on the stimulated Brillouin scattering (SBS), which can effectively improve the detecting depth [14]. The laser is a stable injection-seeded pulsed Nd:YAG laser (Continuum Powerlite Precision II 8000) with a wavelength of 532 nm, a pulse energy of 650 mJ and a repetition rate of 10 Hz. The F-P etalon is a CVI solid etalon made of quartz with a free spectral range (FSR) of 20 GHz and a reflective rate of 99.5%. After calibration [20], the FSR was calibrated to 19.6 GHz. The ICCD system contains an ICCD camera and an ICCD controller. The ICCD camera used was Princeton Instruments PI-MAX II with a resolution of  $1,024 \times 256$ , a pixel size of  $26 \times 26 \mu\text{m}$  and a minimum gate width of 2 ns. The ICCD controller used was Princeton Instruments ST-133. Stanford Research System's DG535 was also used to synchronize the laser with the ICCD system.

The whole procedure is as follow: when the laser pulse comes out, it is diverged to a certain extent by the focus lens. Then, it is focused at a certain depth of the water and the scattering occurs. The backscattering signal is obtained by F-P etalon, and the interference signal is collected by ICCD and finally displayed as 2D interference pattern.

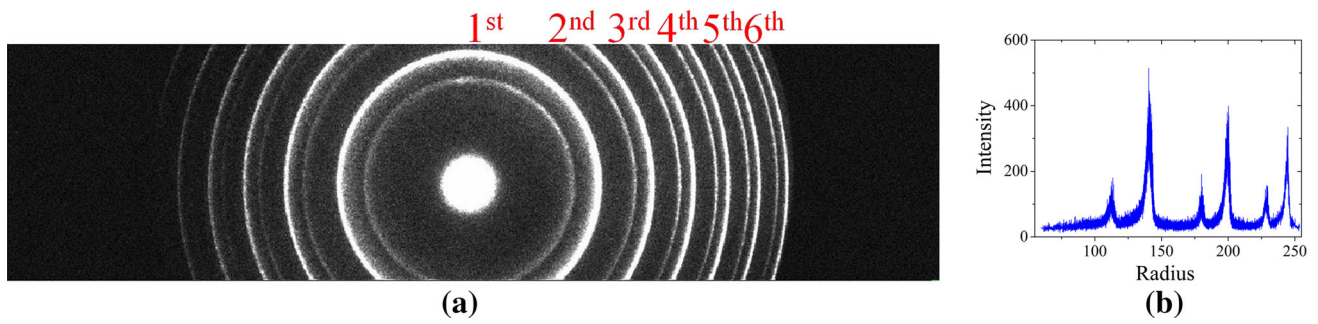


**Fig. 2** **a** Interference pattern taken from the underwater RBS experiment; **b** 1D interference spectrum extracted from the 2D pattern by “data folding”

### 3 Analysis of signal and noise characteristics

Figure 2a is a  $1,024 \times 256$  fringe pattern taken from the stimulated RBS experiment in the clean water (Salinity  $S = 0$ ). The image contains six orders of fringes. Unlike three rings in each order by the spontaneous scattering, the stimulated scattering only has two rings in each order (without the anti-Stokes Brillouin peak): the inner one represents the Stokes Brillouin peaks and the outer one represents the Rayleigh peaks [14]. This pattern can be transformed into 1D spectrum. By using the information such as the position of the peaks and the line shape, the spectrum characteristics can be obtained [13, 15]. However, the resolution of the spectrum is significantly limited by the resolution of ICCD, and each pixel represents a spectrum resolution about 100 MHz. In order to improve the spectrum resolution, a “data folding” process is used [16], after that a spectrum resolution of 1/100 pixel (corresponding to MHz) is achieved, as shown in Fig. 2b.

The first three orders of peaks shown in Fig. 2b are obtained after data folding. The reason for neglecting the 4th to 6th orders is that three orders are sufficient for the measurement of Brillouin shift and linewidth. It can be observed that the folded spectrum is ragged, and the intensities of the darkest pixels are always somewhat above zero.

We tried to directly fit this folded spectrum with a Lorentz profile, which is proved to represent the RBS spectrum in water [15]. The fitted Brillouin shift and linewidth are  $\nu_B = 7.231$  GHz and  $\Gamma_B = 1.087$  GHz, respectively. The temperature calculated by  $\nu_B$  is  $T\nu = 8.40$  °C, and that by  $\Gamma_B$  is  $T\Gamma = 6.89$  °C [21, 22]. However, as the temperature of each experiment should be unchanged,  $T\nu$  and  $T\Gamma$  should be the same in theory. This means that the temperature measurement has a difference of 1.51 °C (corresponding to a Brillouin shift measurement difference of 31 MHz, or a linewidth measurement difference of 96 MHz [21, 22]), which is mainly caused by broadening and noises. To improve the measurement accuracy to MHz, the data folding process is not enough, and it is also a very important

procedure to reduce the influence of broadening and noise. The instrumental broadening is related to the F–P etalon and can be seen as a fixed interference. The noises of ICCD consist of two parts: random shot noise due to the quantum nature of light and the stationary noise due to the dark current of ICCD. With these factors taken into account, the intensity  $I_{out}$  of the image can be expressed as [23, 24]:

$$I_{out} = G \cdot (I_B \otimes B_{instr}) + N_{shot} + N_{dark} \tag{1}$$

where  $G$  is the overall electron gain,  $I_B$  is the Brillouin intensity and is manifested as a Lorentzian function [15]:

$$I_B = \frac{I_0 \cdot \Gamma_B}{\Gamma_B^2 + 4 \cdot (\nu - \nu_B)^2} \tag{2}$$

where  $I_0$  is the maximum value of the RBS spectrum,  $\nu_B$  is the Brillouin shift and  $\Gamma_B$  is the Brillouin linewidth.

$B_{instr}$  is the F–P etalon transmission function, and it can be ideally expressed by an Airy function [25]:

$$B_{instr} = \frac{1}{1 + \frac{4F_R^2}{\pi^2} \cdot \sin^2 \left( \frac{2\pi\mu d\nu}{c} \sqrt{1 - \frac{1}{\mu^2} \cdot \frac{r^2}{f_L^2 + r^2}} \right)} \tag{3}$$

where  $\mu$  is the refractive index of the F–P etalon,  $d$  is the plate spacing of the F–P etalon and  $c$  is the speed of light in vacuum.  $f_L$  is the focus length of the lens, which is used to focus the interference light on the ICCD.  $F_R = \pi R^{1/2}/(1 - R)$  is the finesse of the F–P etalon, and  $R$  is the surface reflectance of F–P etalon. The transmission function will make the received spectrum wider than expected. This influence is shown in Fig. 3: the orange dash dot line represents the instrumental function, the blue dash line represents the ideal Brillouin spectrum and the red solid line is the received spectrum after convolution. As shown here, the instrumental broadening will have minimal effect on Brillouin shift, but will bring obvious error to the measurement of Brillouin linewidth.

The shot noise  $N_{shot}$  is a fundamental property of the quantum nature of light and arises from statistical fluctuations in the number of photons emitted from the object. As the number of scattering photons is very few, the numerical

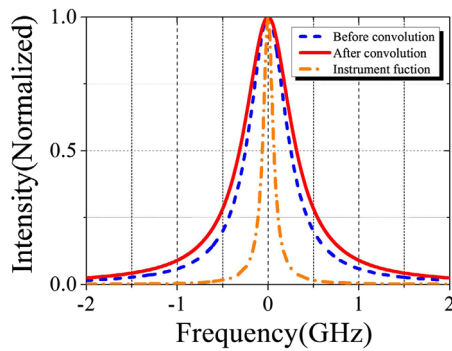


**Fig. 3** The influence of the instrument broadening

differences of the photons received by pixels are significant. The differences are manifested as the intensity fluctuation on image pixels. According to the work by Dussault et al. [23], the noise intensity corresponded with the Poisson distribution:

$$N_{\text{shot}} = G \cdot F \sqrt{\eta \phi_p \tau} \quad (4)$$

where  $F$  is the noise factor introduced by the gain process,  $\eta$  is the quantum efficiency that characterizes the photoelectrons generation process at a given wavelength,  $\phi_p$  is the mean incident photon flux of each pixel and  $\tau$  is the integration time in seconds. This noise is corresponded to the signal intensity of each pixel and manifested as a random noise.

The dark current noise  $N_{\text{dark}}$  is caused by thermally generated electrons in the silicon substrate of the ICCD and is relative with the temperature of each ICCD pixel. It is a uniform stationary noise and can be expressed as a constant. For an ICCD image,  $N_{\text{dark}}$  is manifested as an uplift of the image gray scale, and thus, its effect on the Brillouin linewidth will be much larger than on the Brillouin shift, as the measurement of Brillouin shift is only determined by the positions of Brillouin peak (sensible to shot noise) but not by the height of the peak. The Brillouin linewidth is not only determined by the peak position, but also affected by the intensity of Brillouin peaks, so it is sensible to broadening and the two categories of noises. Therefore, the effect on the measurement of Brillouin shift is analyzed first.

**Table 1** Brillouin shift and linewidth measured by the denoised image in different denoising methods, and the temperatures calculated by them

Methods	$\nu_B$ (GHz)	$\Gamma_B$ (GHz)	$T_V$ (°C)	$T_I$ (°C)	$\Delta T$ (°C)
VST	7.218	1.098	7.76	6.73	1.03
TI-Haar	7.234	1.214	8.54	5.18	3.36

All in all, by combining Eqs. (2–4), Eq. (1) could then be rewritten as:

The analysis of broadening and noise characteristics has shown that the random shot noise will influence the measurement of both Brillouin shift and Brillouin linewidth, and the F–P etalon transmission function and the dark current noise are constant and will only affect the Brillouin linewidth. Therefore, the shot noise should be reduced first to get an accurate Brillouin shift, and then, the fixed broadening and dark noise could be reduced with a fitting procedure.

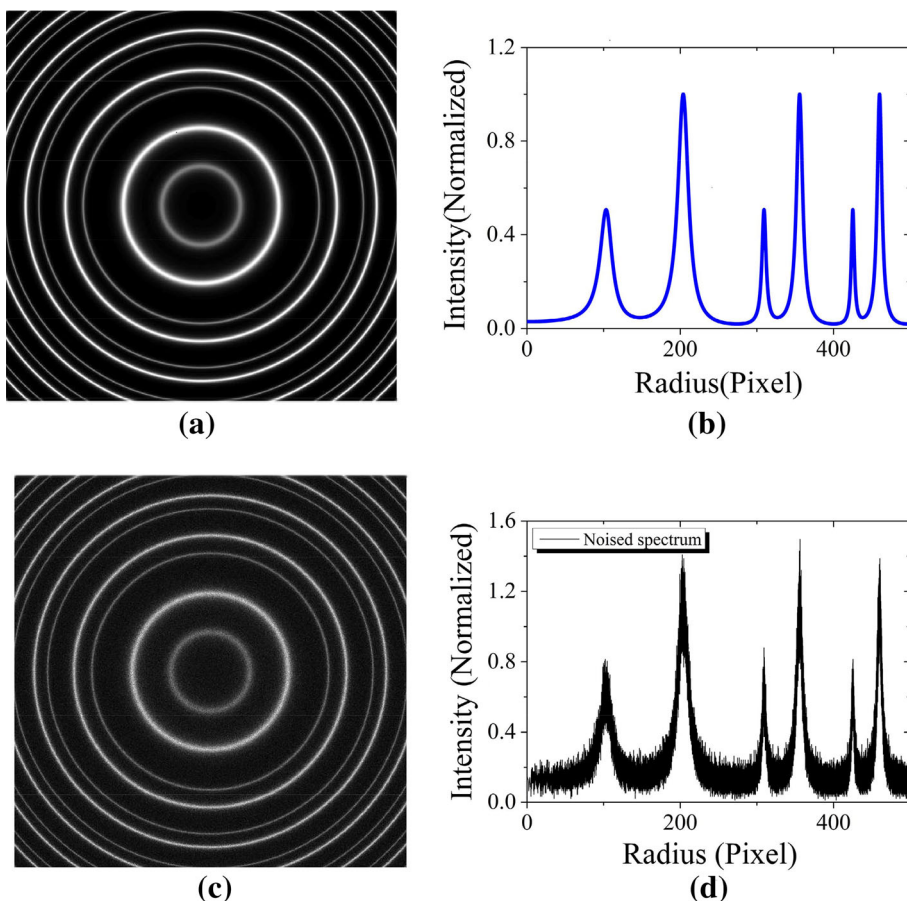
Before using our own method, we have tried to denoise the fringe pattern with two classic methods dealing with Poisson noise in 2D image: the variance stabilizing transformation (VST) [18] wavelet-based denoising method and the translation-invariant Haar (TI-Haar) wavelet-based estimates [19]. Table 1 gives the Brillouin shift and linewidth measured by the denoised image using VST and TI-Haar methods, and the temperatures calculated by them.

$\Delta T$  is the difference between  $T_V$  and  $T_I$ , and it can be seen as the indicator of the measurement error. As shown in Table 1, two methods give measurement errors of more than 1 °C, which corresponds to a more than 20 MHz spectrum measurement error. The reason might be that these methods are aimed for general images, and thus, they do not consider the characteristics of interference patterns. This will lead to significant distortion on the spectrum and bring great error when the shot noise is reduced.

Brillouin shift is determined by the positions of Rayleigh peak and Brillouin peak, and the linewidth is related to the intensity of the Brillouin peak [13, 15]. This means the distortion on the line shape will result in measurement errors of Brillouin shift and linewidth. So the above methods based on the 2D image denoising are not suitable

$$I_{\text{out}}(r) = G \cdot \left( \frac{I_0 \cdot \Gamma_B}{\Gamma_B^2 + 4 \cdot (\nu - \nu_B)^2} \otimes \frac{1}{1 + \frac{4F_B^2}{\pi^2} \cdot \sin^2 \left( \frac{2\pi\mu d\nu}{c} \sqrt{1 - \frac{1}{\mu^2} \cdot \frac{r^2}{f_L^2 + r^2}} \right)} + F \sqrt{\eta \phi_p \tau} \right) + N_{\text{dark}} \quad (5)$$

**Fig. 4** **a** Simulated interference pattern without noise, **b** interference spectrum extracted from (a) by “data folding” method, **c** simulated pattern with noise, **d** interference spectrum extracted from (c) by “data folding” method



for our application, and it is important to develop a new denoising method to reduce shot noise as well as maintain the peak intensity and width of the profile.

The 2D fringe patterns are a series of concentric rings, and it will be more convenient to transfer this 2D image into 1D high resolution spectrum and then try to find a 1D denoising method based on the characteristics of the spectrum. However, there is no prior knowledge of the noise in experimental spectrum. So, in the next step, simulation is given to reconstruct the fringe pattern, and analysis based on the simulation will be carried out to establish a suitable denoising method.

Figure 4a is the simulated interference pattern for clear water RBS, and the F–P etalon broadening is included, but ICCD noise is not added. The center of the fringes is set at the center of the image, and the resolution of the image is  $1,024 \times 1,024$ . The parameters for simulation of the interference pattern are listed in Table 2. Figure 4b is the high resolution spectrum after data folding procedure [16]. Figure 4c is the noised pattern. Figure 4d is the 1D spectrum extracted from Fig. 4c. It can be seen that the simulated spectrum is very similar to experimental data in Fig. 2. It should be noted that the nonuniformity shown in the experimental image is not included in the simulation. This is because we have manually selected the brighter and

**Table 2** Initial parameters for simulation of the interference pattern

Parameter	Value	Parameter	Value
Wavelength	532 nm	$f_L$	0.6 m
Temperature	10 °C	$d$	0.005 m
Resolution	$1,024 \times 1,024$	$\mu$	1.500
Size of the pixel	$26 \mu\text{m} \times 26 \mu\text{m}$	$R$	0.995
$\nu_B$	7.264 GHz	$\Gamma_B$	0.903 GHz
Salinity	0 ‰	FSR	20 GHz

more uniform part from the 2D fringe pattern in the processing procedure, and the nonuniform effect is therefore largely reduced and could be ignored in the simulation.

The simulated noise, which is the difference between Fig. 4b and d, is shown in Fig. 5. The shot noise intensity is related to the signal intensity, and it is obviously larger around peak positions. Denoising methods based on spatial domain (such as mean filter and median filter) cannot be applied to reduce this noise, for the reason that these methods will either be unable to filter the noise on the peaks, or smooth the noise at the cost of distortion of the spectrum line shape. Therefore, we turned to analyze on the Fourier domain. Figure 6 shows the Fourier characteristics of the signal and the shot noise. The dark current noise is

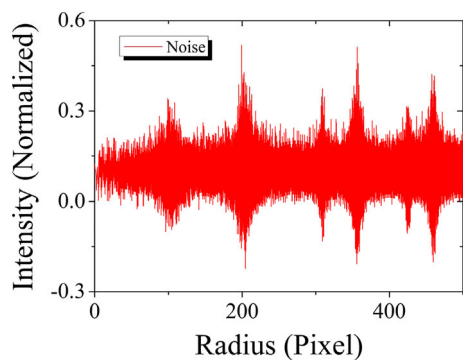


**Fig. 5** The simulated noise

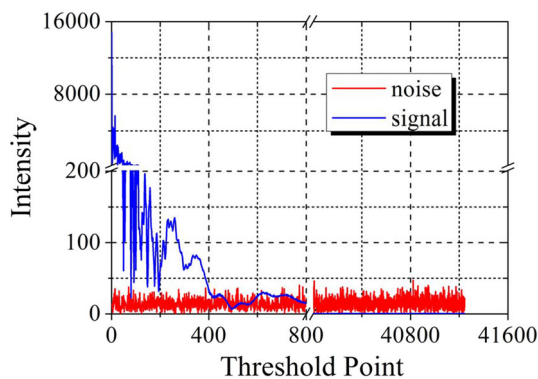


**Fig. 6** Signal spectrum and shot noise spectrum in the Fourier domain

not analyzed here, as the dark current noise is a constant and manifests as a delta function on the zero frequency. The horizontal axis represents the index of sampling points of the discrete Fourier transformation. It can be seen from the figure that the signal intensity mainly concentrates on the low-frequency region and decays rapidly with the increase in the point number, while the shot noise intensity is uniformly distributed on the whole frequency and is far less than the signal on the low-frequency bands. For frequencies beyond the 400th point, the signal begins to be submerged by the shot noise. In the high-frequency region, the shot noise is much larger than the signal. Therefore, the signal and shot noise can be easily distinguished in the Fourier domain, and denoising in the Fourier domain will be helpful to separate the signal from the shot noise.

#### 4 Method for noise and instrumental broadening reduction

As the signal mainly concentrates on the low-frequency region and the shot noise is much larger in the high-frequency region, an intuitive method is to use the ideal low-pass filter for denoising, i.e., reducing the shot noises by

selecting a suitable frequency threshold. The key issue is how to select the filter threshold. If the threshold is too large, the method cannot filter enough shot noise, which will affect the measurement of the Brillouin shift; if the threshold is too low, the method will excessively smooth the spectrum and distort the line shape, especially cut the peaks of the spectrum, which will result in a big measurement error of the linewidth. Figure 7 shows typical results with unsuitable thresholds. In Fig. 7a, the significantly low threshold makes the peaks cut and deeply affects the measurement of the linewidth. In Fig. 7b, the too large threshold introduces too much noise and produces errors on the measurement of the peak positions and the Brillouin shift.

According to the Fourier domain characteristics, the signal intensity decreases to significantly less than the noise intensity after the 500th point, so the optimal threshold should be in the region of 1–500 points. In order to accurately locate the threshold, we conservatively tested all the thresholds in the region of 1–1,000 points. By comparing the Brillouin shifts measured with different thresholds, the performance of each threshold can be evaluated.

Figure 8 shows the Brillouin shifts measured with different thresholds. Each Brillouin shift is measured using the method in [12]. When the threshold is lower than 50 points, measured Brillouin shifts are distributed at the both sides of the initial value and fluctuate severely. This is because the threshold is too low and makes the signal distort. As the threshold increases, the measured value tends to converge. However, when the threshold increases to more than 350 points, the measured value starts to deviate from the initial value, as large threshold introduces much shot noise and makes error for measurement. When the threshold locates in the region of 50–350 points, the measure value fluctuates in the 100 MHz range, which is beyond the MHzs measurement accuracy. This is because the residual shot noise still affects the measurement and brings random disturbance to the Brillouin shift, and it is hard to find a single suitable threshold to completely prevent the effect of the shot noise. In order to reduce the randomness, the mean value of these measured Brillouin shifts is selected as the final Brillouin shift. By averaging, the measured Brillouin shift is 7.266 GHz, which only has an error of 2 MHz with the initial value  $\nu_B = 7.264$  GHz.

The low-pass filter can effectively reduce the shot noise, but cannot remove the broadening or the dark noise, because the broadening is mostly shown in low-frequency region and convoluted with signal; the dark noise is a stationary noise and is located on the lower frequency in the Fourier domain. Other than that the broadening and dark current noise will influence the Brillouin linewidth, so in the following we will analyze them after reducing the shot noise.

**Fig. 7** **a** Smoothing result with threshold of 40th point; **b** smoothing result with threshold of 1,000th point

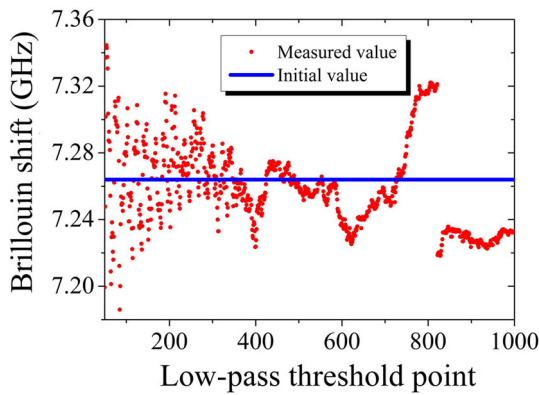
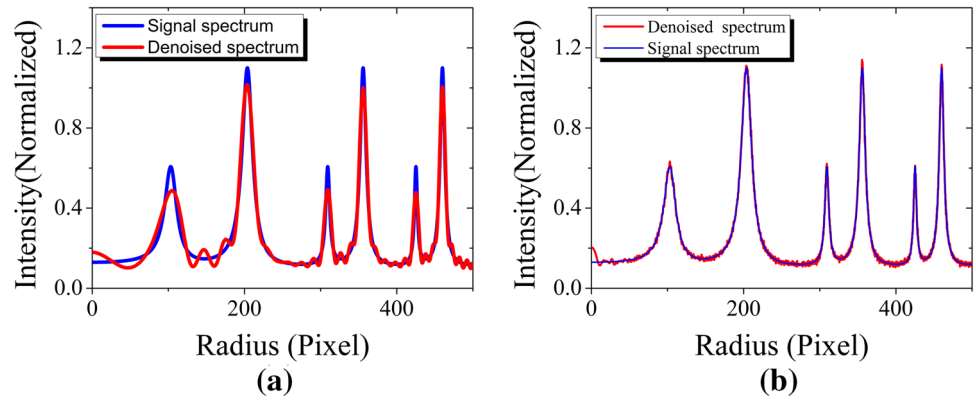


**Fig. 8** Brillouin shifts measured by the interference spectra denoised with different thresholds

Leidecker et al. [17] had theoretically predicted the effect of the F–P etalon instrumental broadening on the spectrum line shape. The methods for removing the broadening include forward modeling (convolution) [20] and backward modeling (deconvolution) [17]. We have tested the forward modeling and the backward modeling method with our experiment data. The results showed that for high resolution spectrum, it is very time-consuming to perform a forward modeling process, while a deconvolution approach after denoising of the shot noise would be much easier. H. W. Leidecker also proved that for etalons with lower instrumental broadening, the deconvolution method could be simplified by a subtraction method, i.e., by directly subtracting the instrumental broadening from the received spectrum, the linewidth could be easily obtained. After reducing the shot noise with low-pass filter, the received spectrum intensity could be expressed as:

$$I_{de}(r) = G \cdot \frac{I_0 \cdot (\Gamma_B + \Gamma_{instr})}{(\Gamma_B + \Gamma_{instr})^2 + 4 \cdot (v - v_B)^2} + N_{dark} \quad (6)$$

where  $I_{de}$  is the interference spectrum after shot noise reduction.  $\Gamma_{instr}$  is the instrumental broadening and is written as[17]:

$$\Gamma_{instr} = \frac{FSR \cdot (1 - R)}{\pi \cdot \sqrt{R} \cdot \cos \theta} \quad (7)$$

The received spectrum is the back-scattered spectrum with a scattering angle of  $\theta = 180^\circ$ . According to simulation condition, the F–P etalon’s  $FSR = 20$  GHz,  $R = 99.5\%$  and the instrumental broadening could be calculated as  $\Gamma_{instr} = 31.9$  MHz. The dark current could not be calculated directly, and instead, it can be fitted using a Levenberg–Marquardt algorithm. With the fitting procedure, the accurate Brillouin linewidth can be measured at the same time. The fitted values of the dark current noise and the Brillouin linewidth in each threshold are shown in Fig. 9.

As shown in Fig. 9, when the threshold is less than 200 points, the spectrum line shape is distorted seriously and the peaks are cut too much. This makes the measured values deviate far away from the initial values. As the threshold increases, the signal is kept more completely and the measured values tend to be close to the initial values. However, when the threshold increases to more than 600 points, the measured values start to deviate from the initial value for the same reason as the measurement of the Brillouin shift. Similarly, the mean values of these measured dark current noise and the Brillouin linewidths are selected as the final values. By averaging, the measured dark current noise is 0.101, and the measured Brillouin linewidth is 0.904 GHz. Compared with the initial values  $N_{dark} = 0.1$ ,  $\Gamma_B = 0.903$  GHz, the measurement errors are  $\Delta N_{dark} = 0.001$  and  $\Delta \Gamma_B = 1$  MHz, respectively.

Some conclusions can be drawn here from the simulation. Since the signal mainly concentrates on the low-frequency region, and the shot noise is uniformly distributed on the whole frequency band, the ideal low-pass filter can effectively reduce the shot noise. By analyzing the Brillouin shifts measured by different thresholds, it can be found that the averaging method can obtain the stable value with MHzs error. When the instrumental broadening is relatively small, the effect of broadening could be simply reduced by subtracting it from the received spectrum. The

**Fig. 9** **a** Dark current noise measured by the interference spectra denoised in the region of 50–1,000 points, **b** Brillouin linewidth measured by the interference spectra denoised in the region of 50–1,000 points

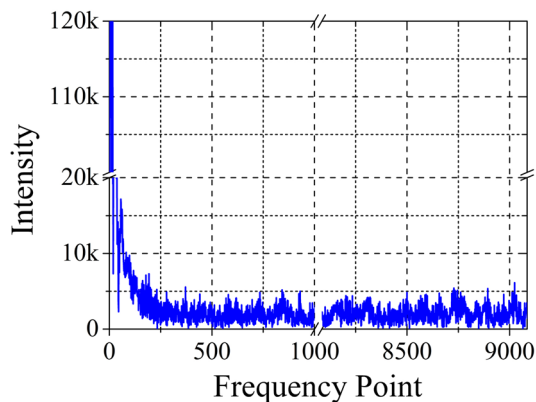
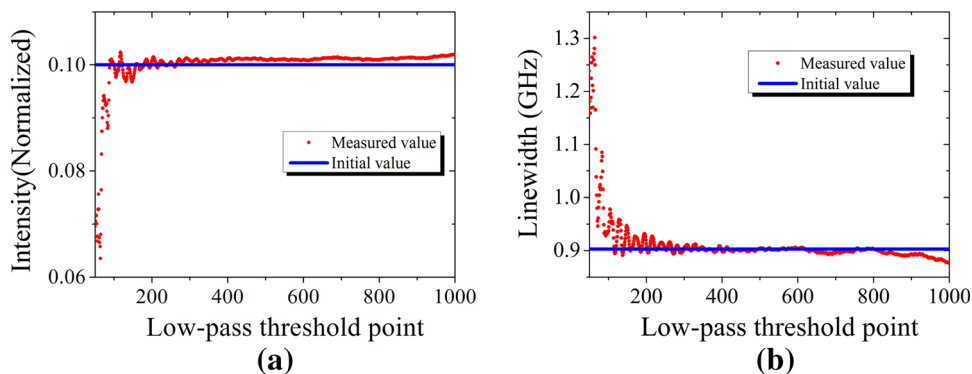


**Fig. 10** Experimental spectrum in the Fourier domain

dark current noise is a constant, and the Brillouin linewidth can be obtained by fitting. Similarly, by averaging method, the stable Brillouin linewidth can be accurately measured in MHzs.

## 5 Experiment results and discussions

The experimental data in Fig. 2 are processed by using the proposed method. Figure 10 shows the Fourier domain spectrum of the data in Fig. 2b.

The broadened signal and the ICCD noise are mixed together; unlike the simulation shown in Fig. 6, we cannot distinguish them in advance; therefore, the selection for the upper frequency point is slightly different. In simulation, we just need to find the point where the signal to noise ratio (SNR) = 1, then choose a conservative region based on this point. In experiment, the mixed Fourier domain intensity becomes stabilized after a certain point, as we know the signal will be submerged by noise in the higher frequency region, we can then assume that after this point, the SNR will be less than 1. For Fig. 10, the intensity becomes stable after 300 points. In order to accurately locate the upper frequency limit, here we conservatively test all the thresholds in the region of 1–500 points.

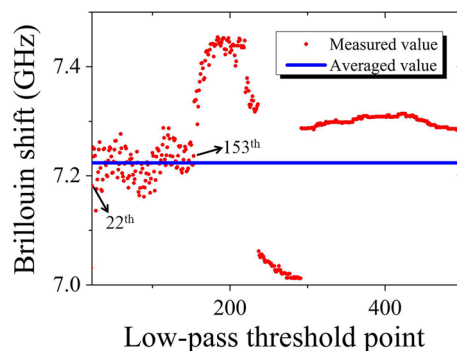


**Fig. 11** Brillouin shifts measured by the interference spectra denoised with different thresholds

The Brillouin shifts measured by different thresholds in the region of 22–500 points are shown in Fig. 11. The 1–21 points are not depicted because large fluctuations are seen. When the threshold increases to more than 22 points, the measured Brillouin shift tends to converge. The measured value starts to deviate from the previous trend and presents gaps after 153th point, which are caused by the excessive shot noise. Therefore, by averaging the measured values in the region of 22–153 points, the final value of Brillouin shift  $\nu_B = 7.224$  GHz, shown as the blue solid line. It can be found that the thresholds for the averaging region for measuring the Brillouin shift are different from those of 50–350 points in the simulation, as each spectrum has its own characteristics in the Fourier domain. Currently, it is recommended to select the threshold region manually, but as certain rules can be drawn for the selection of threshold, we are planning to determine it automatically with a computer program in the future.

According to the experimental setup, the instrumental broadening is calculated as  $\Gamma_{\text{instr}} = 31.4$  MHz. By substituting the measured Brillouin shift into Eq. (6), the fitted dark current noise and Brillouin linewidth are shown in Fig. 12. It can be found that the measured values are stable in the region of 50–219 points. After averaging, the fitted dark current noise  $N_{\text{dark}} = 36.00$  and Brillouin linewidth  $\Gamma_B = 1.011$  GHz.



**Fig. 12** **a** Dark current noise measured by the interference spectra denoised in the region of 22–500 points; **b** Brillouin linewidth measured by the interference spectra denoised in the region of 22–500 points

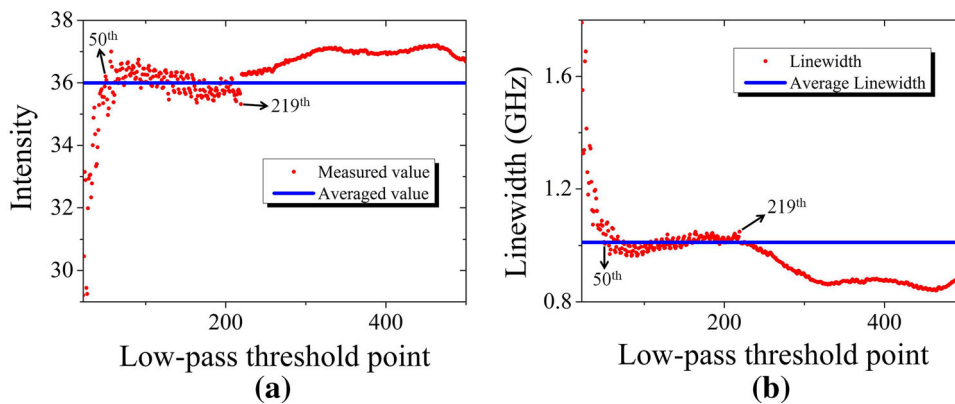


**Table 3** Measured Brillouin shift, linewidth and temperatures calculated by them

	$\nu_B$ (GHz)	$\Gamma_B$ (GHz)	$T_v$ (°C)	$T_T$ (°C)	$\Delta T$ (°C)
Value	7.224	1.011	8.02	8.06	0.04

**Table 4** Temperature and salinity retrieved by the methods in Ref. [26]

	$S_M$ (‰)	$S_C$ (‰)	$\Delta S$ (‰)	$T_m$ (°C)
Value	-0.36 ‰	0 ‰	0.36 ‰	8.14

As described in theoretical considerations, the temperature of each experiment should be unchanged, and  $T_v$  and  $T_T$  should be the same in theory. The temperatures calculated by the measured Brillouin shift and linewidth are shown in Table 3.

In Table 3,  $\Delta T$  is the difference between  $T_v$  and  $T_T$ , i.e., the measurement error. It can be seen that the measurement error of the temperature is 0.04 °C, which corresponds to 1 MHz measurement error of the Brillouin shift or 2 MHz measurement error of the Brillouin linewidth. We also measured the salinity by using these two characteristics and the dual-parameter (temperature and salinity) retrieving method [26]. The retrieved values are listed in Table 4.  $S_M$  is the retrieved salinity, and  $S_C$  is the salinity of the experimental water. The experimental water is clean water where  $S_C = 0$  ‰.  $\Delta S$  is the measurement error of salinity.  $T_m$  is the retrieved temperature by the method. It can be seen from Table 4 that the measured error of salinity is 0.36 ‰, which is within the salinity variance of 0.5 ‰ [21]. On the other hand, the maximum difference between the retrieved temperature  $T_m$  and the measured values in Table 3 is within 0.1 °C, corresponding to the Brillouin shift error of 2 MHz and the linewidth error of 4 MHz. Compared with the 1.51 °C measurement error using direct fitting, the measurement accuracy has been significantly improved. Therefore, both measurements on temperature

and salinity have verified that the proposed method can effectively improve the measurement accuracy of the spectrum characteristics.

In summary, both simulation and experimental results have verified that the proposed method can increase the measurement accuracy of Brillouin shift and linewidth. The measurement accuracy can reach MHz scale, which is greatly improved from tens of MHzs error obtained by directly fitting of the high resolution spectrum. The systematic error of the retrieved temperatures is within 0.1 °C, and the error of the retrieved salinity is 0.36 ‰.

### 6 Conclusion

When the Brillouin lidar system with F–P etalon and ICCD is applied in remote sensing of the ocean physical characteristics, instrumental broadening and noises will seriously affect the measurement of the high resolution spectrum. In this paper, theoretical analysis has proved that the noise is combined with two parts: the shot noise caused by the quantum nature of the scattered light and the dark current noise caused by the thermally generated electrons in ICCD. The instrumental broadening is fixed and related to the F–P etalon used in experiment. We proposed a low-pass method on the Fourier domain for the reduction in the shot noise and the measurement of the Brillouin shift. Then, a fitting procedure considering the instrumental broadening and the dark noise is followed to measure the Brillouin linewidth. Experiment results showed that this processing method can effectively improve the measurement accuracy of Brillouin shift and linewidth from tens of MHz to MHz, corresponding to a temperature accuracy from more than 1 °C to 0.1 °C. This shows great potential in remote sensing applications of the ocean.

In future studies, we will do further research on other denoising methods, such as wavelet denoising. By analyzing the denoising parameters based on characteristics of the noise, we expect that more accurate and convenient

methods can be applied to improve the measurement accuracy in remote sensing of the ocean physical characteristics.

**Acknowledgments** The authors would like to thank National Natural Science Foundation of China (grant No. 61108074 and grant No. 61078062) and Research Fund for the Doctoral Program of Higher Education of China (grant No. 20100142120012). Also, the authors would like to thank Prof. D. Liu for provision of experimental data and his helpful discussions.

## References

1. R.D. Mountain, *Rev. Mod. Phys.* **38**(1), 205–214 (1966)
2. S. Xie, M. Pang, X. Bao, L. Chen, *Opt. Express* **20**(6), 6385–6399 (2012)
3. S. Le Floch, P. Cambon, *J. Opt. Soc. Am. A*: **20**(6), 1132–1137 (2003)
4. Z. Gu, W. Ubachs, *Opt. Lett.* **38**(7), 1110–1112 (2013)
5. B. Witschas, *Appl. Optics* **50**(3), 267–270 (2011)
6. Y. Ma, F. Fan, K. Liang, H. Li, Y. Yu, B. Zhou, *J. Opt.* **14**(9), 095703 (2012)
7. E.S. Fry, J. Katz, D. Liu, T. Walther, *J. Mod. Optic.* **49**(3–4), 411–418 (2002)
8. A. Popescu, K. Schorstein, T. Walther, *Appl. Phys. B-Lasers Opt.* **79**(8), 955–961 (2004)
9. C.L. Korb, B.M. Gentry, C. Weng, *Appl. Opt.* **31**(21), 4202 (1992)
10. W. Gong, J. Shi, G. Li, D. Liu, J.W. Katz, E.S. Fry, *Appl. Phys. B-Lasers Opt.* **83**(2), 319–322 (2006)
11. K. Schorstein, A. Popescu, M. Gobel, T. Walther, *Sensors* **8**(9), 5820–5831 (2008)
12. K. Schorstein, E.S. Fry, T. Walther, *Appl. Phys. B-Lasers Opt.* **97**(4), 931–934 (2009)
13. J. Shi, M. Ouyang, W. Gong, S. Li, D. Liu, *Appl. Phys. B-Lasers Opt.* **90**(3–4), 569–571 (2008)
14. J. Shi, G. Li, W. Gong, J. Bai, Y. Huang, Y. Liu, S. Li, D. Liu, *Appl. Phys. B-Lasers Opt.* **86**(1), 177–179 (2007)
15. L. Zhang, D. Zhang, Z. Yang, J. Shi, D. Liu, W. Gong, E.S. Fry, *Appl. Phys. Lett.* **98**(22), 221106 (2011)
16. J. Huang, Y. Ma, B. Zhou, H. Li, Y. Yu, K. Liang, *Opt. Express* **20**(17), 18568–18578 (2012)
17. H.W. Leidecker Jr, J.T. Lamacchia, *J. Acoust. Soc. Am.* **43**(1), 143–151 (1968)
18. P.R. Prucnal, B.E.A. Saleh, *Opt. Lett.* **6**(7), 316–318 (1981)
19. R. M. Willett, R. D. Nowak, in *Proceedings of 2nd IEEE International Symposium on Biomedical Imaging (IEEE, 2004)*, pp. 1192–1195
20. K. Liang, Y. Ma, J. Huang, H. Li, Y. Yu, *Appl. Phys. B-Lasers Opt.* **105**(2), 421–425 (2011)
21. E.S. Fry, Y. Emery, X. Quan, J.W. Katz, *Appl. Opt.* **36**(27), 6887–6894 (1997)
22. W. Gao, Z. Lv, Y. Dong, W. He, *Chin. Opt. Lett.* **4**(7), 428–431 (2006)
23. D. Dussault, P. Hoess, *Proc. SPIE* **5563**, 195–204 (2004)
24. G. Hernandez, *Appl. Opt.* **5**(11), 1745–1748 (1966)
25. P.A. Wilksch, *Appl. Opt.* **24**(10), 1502–1511 (1985)
26. K. Liang, Y. Ma, Y. Yu, J. Huang, H. Li, *Opt. Eng.* **51**(6), 066002 (2012)